

Scan-Adaptive MRI Undersampling Using Neighbor-based Optimization (SUNO)

Siddhant Gautam, *Student Member, IEEE*, Angqi Li, Nicole Seiberlich, Jeffrey A. Fessler, *Fellow, IEEE*, and Saiprasad Ravishankar, *Senior Member, IEEE*

Abstract—Accelerated MRI involves collecting partial k -space measurements to reduce acquisition time, patient discomfort, and motion artifacts, and typically uses regular undersampling patterns or hand-designed schemes. Recent works have studied population-adaptive sampling patterns that are learned from a group of patients (or scans) based on population-specific metrics. However, such a general sampling pattern can be sub-optimal for any specific scan since it may lack scan or slice adaptive details. To overcome this issue, we propose a framework for jointly learning scan-adaptive Cartesian undersampling patterns and a corresponding reconstruction model from a training set. We use an alternating algorithm for learning the sampling patterns and reconstruction model where we use an iterative coordinate descent (ICD) based offline optimization of scan-adaptive k -space sampling patterns for each example in the training set. A nearest neighbor search is then used to select the scan-adaptive sampling pattern at test time from initially acquired low-frequency k -space information. We applied the proposed framework (dubbed SUNO) to the fastMRI multi-coil knee and brain datasets, demonstrating improved performance over currently used undersampling patterns at both $4\times$ and $8\times$ acceleration factors in terms of both visual quality and quantitative metrics. The code for the proposed framework is available at <https://github.com/sidgautam95/adaptive-sampling-mri-suno>.

Index Terms—Magnetic resonance imaging, sampling pattern optimization, deep learning, image reconstruction, iterative coordinate descent, nearest neighbor search.

I. INTRODUCTION

Magnetic Resonance Imaging (MRI) is a widely used non-invasive biomedical imaging technology that allows visualization of both anatomical structures and physiological functions. Some of its benefits include a lack of ionizing radiation and excellent soft-tissue contrast. MRI scanners sequentially collect measurements in the time (or spatial frequency) domain (known as k -space), from which an image is reconstructed. The scanner must sample numerous k -space points in order to estimate an image with a clinically appropriate spatial resolution, which causes the acquisition process to be slow

and expensive. Accelerating MRI scans reduces acquisition time, reduces patient discomfort, increases scaling throughput, and reduces motion artifacts. Such acceleration often requires choosing an appropriate undersampling pattern or trajectory along with a reconstruction model that enables accurate recovery from reduced measurements.

Some of the earliest approaches for accelerating MR imaging included pulse sequence and k -space trajectory design [1]–[3] and parallel imaging [4]–[6], which exploits the spatial information available when using an array of receiver coils. Parallel imaging offers hardware-based acceleration but often suffers from increased noise and imperfect artifact correction at higher undersampling rates. It is limited to smaller acceleration factors because of imperfect artifact correction and higher noise at higher acceleration rates.

Compressed sensing (CS) [7], [8] has been widely used to enable the reconstruction of MR images from a reduced set of measurements. Traditional MRI follows the Nyquist-Shannon theorem, requiring dense sampling in k -space. However, according to CS theory, the k -space sampling can be done at sub-Nyquist rates and the image can be reconstructed using prior knowledge of sparsity in some transform domain [8]–[11] when the sampling operator and sparsity basis are sufficiently incoherent. Some of the widely used undersampling patterns in CS-MRI include variable density [12], Poisson-disc [13], combined variable density and Poisson disc [14], and equispaced Cartesian with skipped lines [15]. Recently, approaches using learned image models for reconstruction have also been explored. These methods include techniques such as synthesis dictionary learning [16]–[19] and transform learning [20], [21].

With the advent of deep learning, convolutional neural networks (CNNs) have achieved tremendous success in reconstructing MR images from undersampled measurements. Some of these approaches have used U-Net architectures [22] by training them in a supervised manner to remove artifacts in aliased images [23]. Similarly, variational networks have been used to solve the image reconstruction problem for accelerated multi-coil MRI by combining neural networks with the MR forward model [24], [25]. Other works in deep learning-based MRI reconstruction include ADMM-Net [26] and GANs [27]. Recently, MoDL [28] has become quite popular in solving the MRI reconstruction problem, in which the MRI forward model is used within a data consistency term, and a CNN reconstructor is used as a denoiser to regularize the reconstruction.

One of the first works to optimize MRI undersampling

This work was supported by NIH Grant R21 EB030762.

S. Gautam and A. Li are with the Department of Computational Mathematics, Science and Engineering, Michigan State University, East Lansing, MI 48824 USA (e-mail: gautamsi@msu.edu; liangq1@msu.edu).

N. Seiberlich is with the Department of Radiology, University of Michigan, Ann Arbor, MI 48109 USA (e-mail: nse@med.umich.edu).

J. A. Fessler is with the Department of Electrical and Computer Engineering and Department of Biomedical Engineering, University of Michigan, Ann Arbor, MI 48109 USA (e-mail: fessler@umich.edu).

S. Ravishankar is with the Department of Computational Mathematics, Science and Engineering and the Department of Biomedical Engineering, Michigan State University, East Lansing, MI 48824 USA (e-mail: ravisha3@msu.edu).

patterns used training k -space data and reconstruction error as the training loss to optimize a single pattern over training scans [29]. Subsequent work on sampling optimization designed adaptive sampling patterns using the power spectra of the reference k -space data [30], [31] or the energy preserving sampling method [32]. Statistical experiment design techniques for MRI sampling prediction were proposed that used the Cramer-Rao lower bound [33], [34]. Later, the greedy algorithm and its variations were used to learn a single population-adaptive sampling pattern over a training set of images with a specific choice of reconstruction method [35], [36]. Since these approaches learn the undersampling pattern using greedy algorithms over a large number of images, the computational cost involved is high, and it scales quadratically with the number of lines in the mask. To avoid this, a stochastic version of the greedy mask learning algorithm was proposed that resolved the scaling issues of the previous greedy approaches [37].

Recently, deep learning approaches were proposed that jointly learn a sampling pattern and a corresponding trained reconstruction network [38]–[46]. LOUPE [38] and its multi-coil extension [39] determine the probability of sampling each pixel or row/column in the k -space domain. Its underlying parameters are learned jointly with those of the reconstructor (U-Net). Similarly, J-MoDL [40] jointly learns an MoDL reconstruction network and a sampling pattern whose parameters are optimized separately along the row and column directions. Subsequent works, such as SeqMRI [43], used a reconstruction model trained jointly with a sampler that predicts sampling patterns sequentially. MNet [45] also explored jointly training a reconstruction network and a CNN-based sampler to predict the undersampling pattern directly from low-frequency k -space information. For parallel MRI, bias-accelerated subset selection (BASS) [42], [44], a subset selection method for learning sampling patterns, which gives a fast way to learn sampling patterns. More recently, AutoSamp [46] is one of the recent deep learning methods proposed for joint optimization of sampling patterns and reconstruction for 3D MRI that uses variational information maximization.

These works can be divided into those predicting Cartesian undersampling patterns [38], [42]–[46] and the ones learning non-Cartesian patterns [40]. Other recent works for learning non-Cartesian sampling trajectories include PILOT [47], SPARKLING [48], [49], BJORK [50], NC-PDNet [51], and SNOPI [52].

Sequential decision processes have also been applied to undersampling prediction, where they sequentially learn MRI sampling patterns using reinforcement learning. In these problems, the sampling optimization is formulated as a partially observable Markov decision process (POMDP) [53], [54].

One limitation of the more common population-adaptive approaches [35], [38], [40], [42], [44] is that they learn a sampling pattern suited to the entire dataset rather than to individual scans. Implementing scan-adaptive sampling prediction (e.g., SeqMRI [43], M-Net [45]) could potentially enhance sampling efficiency by leveraging key slices or image-specific features and thus improve reconstruction performance compared to population-adaptive methods. The population-

adaptive designs can be learned off-line, whereas scan-specific sampling patterns must be determined rapidly while the subject is in the scanner, after collecting some preliminary k -space data.

This paper proposes a framework for jointly learning scan-adaptive 1D Cartesian undersampling patterns and a reconstruction model for multi-coil MRI on a training dataset. Our algorithm alternately estimates a reconstructor and a collection of sampling patterns from training data. We use a sampling optimization algorithm based on iterative coordinate descent to yield improved sampling patterns on training data and use the nearest neighbor search to determine such patterns at test time based on acquired low-frequency k -space. The key methodological difference between the proposed SUNO framework and recent scan-adaptive methods like SeqMRI [43] (or e.g., M-Net [45]) is that the SeqMRI employs a fully differentiable approach, jointly optimizing a sequential sampling policy and a reconstruction strategy via standard backpropagation. In contrast, SUNO formulates mask learning as an integer programming problem and uses a dictionary of learned sampling patterns to find the best mask at test time. Our results show that the scan-adaptive Cartesian sampling patterns yield better reconstruction quality in terms of NRMSE, SSIM [55], and PSNR metrics, compared to existing baselines for multi-coil MRI. Moreover, at test time, we also explored efficiently learning local (scan-adaptive) reconstruction networks from small clusters in the training set for each test image. The network is trained with images that are in the local neighborhood of the initial test reconstruction [56]. This paper builds upon our previous short conference work [57] and extends it to higher acceleration factors and learns undersampling patterns over different anatomies. We also present results with scan-adaptive reconstructors along with extended comparisons with several baselines.

The rest of this paper is organized as follows. Section II discusses the details of the MRI forward model, deep learning-based reconstruction, and the details of our proposed training framework that alternates between optimizing a reconstructor and updating scan-adaptive sampling patterns on a training set. Section III discusses the details of training datasets and implementation details. Section IV presents the results of applying our approach to the fastMRI dataset and compares it with existing baselines. We also provide ablation studies on our sampling pattern optimization algorithm. Section V provides a summary of our findings and possible new directions for future work and further conclusions are provided in Section VI.

II. METHODS

A. Multi-coil MRI Reconstruction

In multi-coil MRI, the goal is to recover the underlying MR image $\mathbf{x} \in \mathbb{C}^n$ from a set of undersampled multi-coil measurements $\mathbf{y} \in \mathbb{C}^m$. The regularized MRI reconstruction problem can be formulated as follows:

$$\min_{\mathbf{x}} \|\mathbf{M}\mathbf{A}\mathbf{x} - \mathbf{y}\|_2^2 + \lambda\mathcal{R}(\mathbf{x}) \quad (1)$$

Here, \mathbf{M} is an operator that subsamples k -space, $\mathbf{A} = \mathbf{F}\mathbf{S}$ is the fully sampled MRI measurement operator and $\mathcal{R}(\mathbf{x})$

is a regularizer. \mathbf{F} is the 2D Fourier transform operator and \mathbf{S} encodes the sensitivity maps of the receiver coils. The regularizer $\mathcal{R}(\mathbf{x})$ typically captures assumed properties of the image and can take on various forms such as total variation, or low-rank or transform-domain sparsity penalties.

Recently, deep learning has become an increasingly powerful tool for solving MRI reconstruction problems. These methods have the advantage that they do not need hand-crafted regularizers. In this paper, we leverage four such deep learning techniques that have been proposed for solving MRI reconstruction problems:

- 1) U-Net [22] is a deep convolutional network that has been used to predict the underlying clean image from the aliased image as follows:

$$\hat{\mathbf{x}} = D_{\theta}(\mathbf{A}^H \mathbf{y}), \quad (2)$$

where $\hat{\mathbf{x}}$ is the reconstructed image and D_{θ} is the reconstruction network (U-Net) with learnable parameters θ .

- 2) Model-based deep learning (MoDL) [28] combines deep learning priors with physics-based priors to solve the reconstruction problem. The optimization problem in this case is as follows:

$$\hat{\mathbf{x}} = \arg \min_{\mathbf{x}} \|\mathbf{M}\mathbf{A}\mathbf{x} - \mathbf{y}\|_2^2 + \lambda \|\mathbf{x} - D_{\theta}(\mathbf{x})\|_2^2, \quad (3)$$

where $D_{\theta}(\mathbf{x})$ is a denoiser (CNN) with learnable parameters θ . MoDL tackles (3) by introducing an auxiliary variable \mathbf{z} and adopting an alternating algorithm as follows:

$$\mathbf{x}_{n+1} = \arg \min_{\mathbf{x}} \|\mathbf{M}\mathbf{A}\mathbf{x} - \mathbf{y}\|_2^2 + \lambda \|\mathbf{x} - \mathbf{z}_n\|_2^2 \quad (4)$$

$$\mathbf{z}_n = D_{\theta}(\mathbf{x}_n) \quad (5)$$

Here, \mathbf{x}_{n+1} is the estimated image at $n + 1$ iteration. The alternating scheme is unrolled for a few iterations, and the denoising network is trained end-to-end.

- 3) End-to-End Variational Networks for Accelerated MRI Reconstruction (E2E-VarNet) [25] proposes an end-to-end deep learning framework for accelerated multi-coil MRI reconstruction. Instead of reconstructing images directly from undersampled k -space data, VarNet unrolls an iterative optimization inspired by variational methods [24], alternating between data consistency and learned image-domain regularization. Each iteration updates the k -space data using both the measured values and a CNN-based prior applied in the image domain. The reconstruction task is, thus, formulated as minimizing the following variational objective:

$$\hat{\mathbf{x}} = \arg \min_{\mathbf{x}} \{\|\mathbf{M}\mathbf{A}\mathbf{x} - \mathbf{y}\|_2^2 + \lambda \mathcal{R}(\mathbf{x})\}, \quad (6)$$

where $\mathcal{R}(\mathbf{x})$ is a learned regularization function. Each update is performed in k -space via:

$$\mathbf{k}^{(i+1)} = \mathbf{k}^{(i)} - \alpha_i (\mathbf{M}(\mathbf{k}^{(i)} - \mathbf{y}) + \mathbf{A} \text{CNN}(\mathbf{A}^H \mathbf{k}^{(i)})), \quad (7)$$

where $\mathbf{k}^{(i)}$ is the k -space estimate at iteration i ; \mathbf{A} and \mathbf{A}^H are the fully-sampled forward and adjoint

operators. CNN is a learned regularizer (network) acting in image space. The values of step size α_i as well as the parameters of the CNNs are learned from data. The corresponding reconstructed image at the final step, from the k -space estimate $\hat{\mathbf{k}}$ can be given as:

$$\hat{\mathbf{x}} = \mathbf{A}^H(\hat{\mathbf{k}}). \quad (8)$$

- 4) Zero-Shot Self-Supervised Learning for MRI Reconstruction (ZS-SSL) [58] uses self-supervised learning to train a model directly on undersampled MRI data from individual scans, enabling scan-specific reconstructions without relying on fully-sampled measurements or extensive databases. ZS-SSL employs a partitioning of k -space data that enables scan-specific self-supervised training as well as validation with a clear stopping criterion.

The above expressions are for a fixed or a population-adaptive sampling pattern \mathbf{M} . However, in this paper, we focus on learning scan-specific sampling patterns $\{\mathbf{M}_i\}$ instead of a single population-adaptive sampling pattern. In this framework, we first optimize these scan-adaptive masks $\{\mathbf{M}_i\}$ offline for the training set. Then at test time, these masks are chosen using a nearest neighbor search, as described in a later subsection.

B. Framework for Jointly Learning Reconstructor and Sampler

This section presents our proposed approach for jointly learning a set of scan-adaptive Cartesian undersampling patterns $\{\mathbf{M}_i\}$ along with a reconstructor trained to be suitable for all of these undersampling patterns. Using a training set consisting of fully sampled k -space and corresponding ground truth images, we learn a collection of scan-adaptive sampling masks and a reconstructor from the training data. We formulated the joint optimization problem as follows:

$$\min_{\theta, \mathbf{M}_i \in \mathcal{C}, i \in \{1, \dots, N\}} \sum_{i=1}^N \|f_{\theta}(\mathbf{A}_i^H \mathbf{M}_i \mathbf{y}_i^{\text{full}}) - \mathbf{x}_i^{\text{gt}}\|_2^2, \quad (9)$$

where $\mathbf{M}_i \in \mathcal{C}$ is the i th training k -space subsampling mask that inserts zeros at non-sampled locations, $\mathbf{y}_i^{\text{full}}$ and \mathbf{x}_i^{gt} are the i th fully sampled multi-coil training k -space and the corresponding ground truth image, respectively and N is the number of training images. The set \mathcal{C} denotes all the 1D Cartesian undersampling patterns with a specified sampling budget. \mathbf{A}_i^H is the adjoint of the fully sampled multi-coil MRI measurement operator for the i th training scan, and f_{θ} is the reconstruction network trained on the set of sampling patterns $\{\mathbf{M}_i\}$.

We use the alternating framework shown in Figure 1 to solve this highly challenging optimization problem. The algorithm starts with variable density random sampling (VDRS) masks as an initial guess [8] and alternates between updating a reconstructor and sampling masks until we get a final set of scan-adaptive masks $\{\mathbf{M}_i\}$ and a reconstruction network f_{θ} trained on them. For optimizing the scan-adaptive masks, we initially use a greedy [35] and later our proposed ICD-based

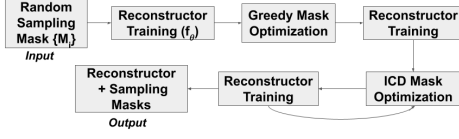


Fig. 1: Alternating framework for mask and reconstructor update during joint training. The first four steps serve to create a good initialization for the mask and reconstructor optimization. The masks could be alternatively initialized with, e.g., population-adapted patterns.

sampling optimization algorithm. More details of the sampling optimization algorithm are in the next section.

C. Iterative Coordinate Descent (ICD) based Sampling Optimization

A greedy algorithm was proposed in prior work [35] to optimize high-quality sampling patterns that specify samples in k -space that minimize the reconstruction error given a choice of the reconstruction model used. Starting with no sampled lines or only fixed low-frequency lines, at each step of the greedy sampling optimization, the k -space phase encoding line that gives the lowest reconstruction error is added to a particular sampling mask. The algorithm keeps adding lines until the sampling budget is reached. However, the sampling pattern obtained using the greedy algorithm can be sub-optimal and can be further optimized using an iterative coordinate descent (ICD) based sampling optimization. The proposed iterative coordinate descent (ICD) based sampling optimization algorithm further optimizes the greedy mask iteratively by picking one line at a time in the current mask and moving it to the best new location in terms of the reconstruction error, and cycling over all lines to move in this manner. Figure 2 shows the schematic of mask updates during various steps of the ICD sampling optimization. The steps of the algorithm are given in detail in Algorithm 1. Thus, the ICD sampling optimization further improves the greedy masks and yields better quality scan-adaptive masks. The optimized masks depend on the choice of the initial mask, the reconstructor used, and the metric chosen for the loss function. The ICD sampling optimization algorithm ensures a monotonic decrease and convergence of the non-negative reconstruction loss (9).

D. Neighbor based Sampling Prediction

This subsection describes our approach to predict the sampling pattern from initially acquired k -space measurements at testing time. Given our set of scan-adaptive sampling patterns obtained from the training process, the task at test time is to estimate the high-frequency lines in k -space based on initially acquired low-frequency information. We use the nearest neighbor search to predict the sampling pattern from the collection of training scans. The nearest neighbor is found by comparing the adjoint reconstruction of the low-frequency test k -space and the corresponding low-frequency part of the training k -space as follows:

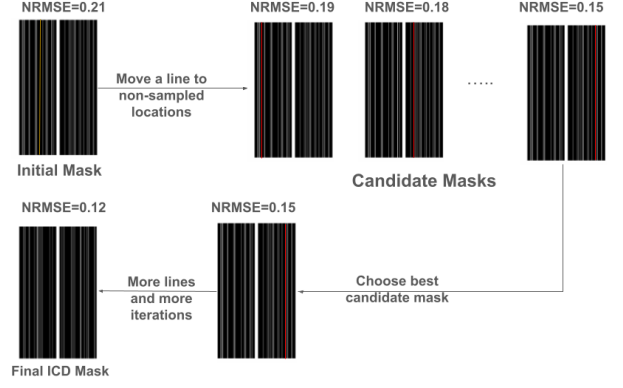


Fig. 2: Schematic of offline iterative coordinate descent (ICD) based sampling pattern optimization.

Algorithm 1 Sampling Pattern Optimization

Require: Fully sampled k -space \mathbf{y}^{full} and corresponding forward operator \mathbf{A} , ground truth image \mathbf{x}^{gt} , reconstructor f , loss function L , budget B , number of ICD iterations N_{iter} , set of all possible line locations \mathbf{S} , set of locations of initial sampled lines Ω_{initial} , initial mask $\mathbf{M}_{\Omega_{\text{initial}}}$

- 1: $\Omega \leftarrow \Omega_{\text{initial}}$
- 2: **for** $j = 1 : N_{\text{iter}}$ **do**
- 3: $\{l_i\}_{i=1}^B \leftarrow$ entries in current Ω
- 4: **for** $i = 1 : B$ **do**
- 5: $\Omega' = \Omega \setminus l_i$
- 6: $\Omega \leftarrow \Omega' \cup S^*$ where

$$S^* = \arg \min_{S \in \mathbf{S}, S \neq \Omega'} L(\mathbf{x}^{\text{gt}}, f(\mathbf{A}^H \mathbf{M}_{\Omega' \cup S} \mathbf{y}^{\text{full}}))$$

where $\mathbf{M}_{\Omega' \cup S}$ is the operator sampling along lines at $\Omega' \cup S$.

- 7: **end for**
 - 8: **end for**
 - 9: **return** Ω
-

$$d_i = d(\mathbf{A}_{\text{test}}^H \mathbf{y}_{\text{test}}^{\text{lf}}, \mathbf{A}_{\text{train}_i}^H \mathbf{y}_{\text{train}_i}^{\text{lf}}), \quad (10)$$

where $\mathbf{y}_{\text{test}}^{\text{lf}}$ and $\mathbf{y}_{\text{train}_i}^{\text{lf}}$ are the low-frequency part of testing and training k -space with zeros at high frequencies. $\mathbf{A}_{\text{test}}^H$ and $\mathbf{A}_{\text{train}_i}^H$ are the adjoints of the fully sampled MRI forward operators for the test and i th training scans, respectively. Different metrics d can be used to define the nearest neighbors, e.g., Euclidean distance, structural similarity index (SSIM) [55], or normalized cross-correlation. We choose the optimized mask of the nearest neighbor (called the SUNO mask) and use that at test time in the scanner to collect the rest of the measurements.

E. Local Neighbor-based Reconstructor Training

Adaptive local network training [56] on a set of nearest neighbors can yield better reconstructions compared to a network that is trained globally on all the images in the training set. This is because the local reconstructor is trained on a dataset closely resembling the underlying test image, rather than on a large and diverse training set. As a result, it

adapts more effectively to similar or related image features and provides a better fit than a model trained on many unrelated scans. We apply this framework to our SUNO masks and train a local network in addition to a reconstruction network trained globally (i.e., on a large training set). We call the approach with the locally trained reconstruction network “SUNO-Local” and the one with the global network “SUNO-Global” in the rest of the paper. Mathematically, the problem of finding the nearest neighbors for local training can be formulated as:

$$\hat{C}_{\mathbf{x}} = \arg \min_{C \in \mathcal{C}, |C|=k} \sum_{n \in C} d(\hat{\mathbf{x}}, \mathbf{x}_n), \quad (11)$$

where $\hat{\mathbf{x}}$ is an initial reconstructed image, \mathbf{x}_n is the n th ground truth from the training set and d is the distance metric used to evaluate neighbors. C is the set of nearest neighbors with cardinality k and \mathcal{C} denotes the set of all such sets with k elements. We computed the initial reconstructed image using the MoDL network (which is trained globally) on the test k -space undersampled by the SUNO mask. Euclidean distance is used as the similarity metric above. The local network is trained for only a few epochs (e.g., using the ADAM optimizer). A smaller learning rate is used to prevent overfitting on the smaller training set of nearest neighbors.

III. EXPERIMENTS

A. Datasets

Our experiments used the fastMRI multi-coil knee and brain datasets [59], [60]. The details for each dataset are as follows:

1) *fastMRI Multi-coil Knee Dataset*: The fastMRI multi-coil knee dataset contains images collected using two different pulse sequences, yielding coronal proton-density weighted images with (PDFS) and without (PD) fat suppression. For our experiments, we used a total of 156 scans (comprising both PD and PDFS scans) and split them into training, validation, and testing sets. From each scan, we discarded the first 10 and last 5 slices due to a lack of identifiable image features, which gave us 1514, 194, and 104 training, validation, and testing slices, respectively. Each image was collected using 15 coils of k -space data with a matrix size of 640×368 . We used the ESPIRiT calibration approach [61] to estimate the sensitivity maps from the central 30 lines of k -space.

2) *fastMRI Multi-coil Brain Dataset*: To test the generalization of our proposed sampling prediction algorithm, we also applied our algorithm on the fastMRI multi-coil brain dataset that consists of FLAIR, T1-weighted, and T2-weighted images. From this dataset, we used a total of 1660 slices for our experiments and split them into 1480, 120, and 60 training, validation, and testing images, respectively. The scans were acquired with a matrix acquisition size of 640×320 , and the number of receiver coils varied between 4 and 20 across different scans. The sensitivity maps were estimated using the ESPIRiT calibration approach.

B. Comparison with Other Undersampling Patterns

We compared our proposed SUNO sampling patterns with low-frequency (LF) sampling, variable density random sampling (VDRS) [8], equispaced masks [15], trained

scan-adaptive SeqMRI [43], and trained population-adaptive LOUPE [38] masks (all Cartesian). For the SeqMRI and the LOUPE methods, we used their publicly available PyTorch implementations¹ and extended them to the multi-coil setting. For the LOUPE code, we set the slope parameter $\alpha = 5$ and used a learning rate of 10^{-3} to update the mask parameters. For the SeqMRI code, we used a learning rate of 5×10^{-5} , with a decay ratio set to 0.5, which was applied every 10 epochs. The number of sequential steps in the model was set to 4. The SSIM between real-valued, magnitude-only images was used as the loss function to evaluate reconstruction quality during training. For LOUPE, a two-channel standard U-Net was used as the reconstruction model, whereas SeqMRI employed a two-channel residual U-Net. Both networks had 64 channels in the first layer and were trained for 100 epochs. For each undersampling pattern, 30 and 15 lines were fixed in the central low-frequency part for $4\times$ and $8\times$ undersampling factors, respectively. Figure 3 shows the obtained SUNO mask along with other baseline masks for the knee dataset. Separate undersampling patterns were optimized and estimated using nearest neighbor search for the brain dataset. In this work, we focus only on learning and comparing to other Cartesian undersampling baselines. Table I gives the parameters used inside the sampling optimization algorithm for each acceleration factor. The number of iterations of Algorithm 1 N_{iter} was set to 1 since the most loss change happens in the first iteration and after that, changes are smaller but with increased computation.

Acceleration Factor	$4\times$	$8\times$
Budget (B)	92	46
Lines fixed at center (F)	30	15
Lines to be optimized ($B - F$)	62	31
Search Space ($W - F$)	338	353
No. of ICD iterations N_{iter}	1	1

TABLE I: Parameters involved in the sampling optimization algorithm for the fastMRI multi-coil knee dataset with k -space dimension 640×368 . 1/3rd of the lines are fixed at the center of k -space, and the rest of the lines are optimized by the algorithm. The k -space dimensions for the brain dataset are different (640×320), so the rest of the parameters scale accordingly.

C. Implementation Details

Our algorithms were implemented in Python, using the PyTorch package. We used two-channel reconstruction networks to obtain the underlying image from the undersampled k -space, with the two channels being the real and imaginary parts of the complex image. We used Facebook Research’s implementation of U-Net in the PyTorch framework². For MoDL [28], we used a deep iterative up-down (DIDN) network [62] as the denoiser inside the training framework. We used 6 unrollings of the denoiser and the conjugate gradient (CG) block. The regularization parameter λ controlling the weighting of the two terms (see Eq.(3)) was set to 10^2 and

¹<https://github.com/tianweiy/SeqMRI>; <https://github.com/caglabahadir/LOUPE>

²<https://github.com/facebookresearch/fastMRI/blob/main/fastmri/models/unet.py>

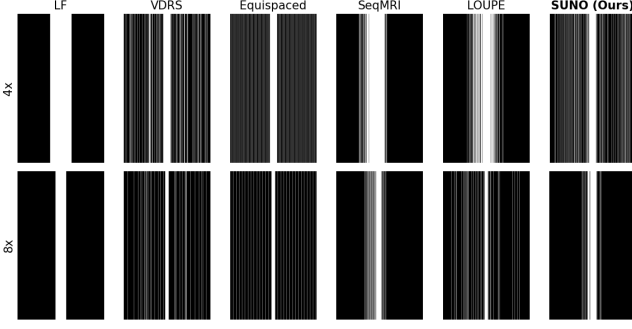


Fig. 3: Comparison of different masks used for reconstruction at a) $4\times$ and b) $8\times$ acceleration factors for the knee dataset. Masks displayed are: 1) low-frequency (fixed), 2) VDRS (random), 3) Equispaced (fixed), 4) SeqMRI (optimized - scan adaptive), 5) LOUPE (optimized - population adaptive), and 6) SUNO (optimized - scan adaptive).

the tolerance for the CG algorithm used was 10^{-5} after tuning them on multiple images. For VarNet [25], we used 12 cascades, each containing a U-Net with 18 channels in the first layer, using the official implementation provided by Facebook Research.³ Sensitivity maps used for VarNet training were estimated using the ESPIRiT calibration approach [61]. The reconstructed image was obtained by applying the adjoint of the forward MRI operator to the reconstructed k -space from VarNet. Both MoDL and VarNet were trained for 100 epochs with a batch size of 1. Adam optimizer [63] was used for training the networks with a learning rate of 10^{-3} . For the ZS-SSL approach [58], we employed 10 unrolled blocks and 15 residual blocks, along with 10 conjugate gradient iterations for data consistency. The model was trained for 300 epochs with a learning rate of 5×10^{-4} using the official implementation available on GitHub.⁴ The simulations were performed on an NVIDIA RTX A5000 GPU with 24 GB RAM. For the local training, the MoDL network was trained on the 30 nearest neighbors for 30 epochs. A learning rate of 10^{-6} was used to prevent overfitting in this case since the training set was small. All the training multi-coil k -space data were undersampled by the predicted SUNO mask specific to the local training configuration.

D. Performance Metrics

To evaluate the quality of reconstructed images, we used normalized root mean squared error (NRMSE), structural similarity index (SSIM) [55], and peak signal-to-noise ratio (PSNR) as the metrics. These metrics assess the similarity between the ground truth and the reconstructed images. Lower NRMSE, higher SSIM and PSNR values suggest better reconstruction quality. All the metrics were evaluated on the central 320×320 portion of the image. Their mathematical expressions can be given by

$$\text{NRMSE}(\mathbf{x}, \hat{\mathbf{x}}) = \frac{\|\mathbf{x} - \hat{\mathbf{x}}\|_2}{\|\mathbf{x}\|_2}, \quad (12)$$

$$\text{SSIM}(\mathbf{x}, \hat{\mathbf{x}}) = \frac{(2\mu_{\mathbf{x}}\mu_{\hat{\mathbf{x}}} + c_1)(2\sigma_{\mathbf{x}\hat{\mathbf{x}}} + c_2)}{(\mu_{\mathbf{x}}^2 + \mu_{\hat{\mathbf{x}}}^2 + c_1)(\mu_{\mathbf{x}}^2 + \mu_{\hat{\mathbf{x}}}^2 + c_2)}, \quad (13)$$

$$\text{PSNR}(\mathbf{x}, \hat{\mathbf{x}}) = 10 \log_{10} \frac{\max(|\mathbf{x}|)^2 d}{\|\mathbf{x} - \hat{\mathbf{x}}\|_2^2}, \quad (14)$$

where \mathbf{x} and $\hat{\mathbf{x}}$ are the ground truth and reconstructed images, respectively, and d is the total number of pixels in the image. $\mu_{\mathbf{x}}$ and $\mu_{\hat{\mathbf{x}}}$ are the mean of images \mathbf{x} and $\hat{\mathbf{x}}$, $\sigma_{\mathbf{x}}^2$ and $\sigma_{\hat{\mathbf{x}}}^2$ are their respective variances and $\sigma_{\mathbf{x}\hat{\mathbf{x}}}$ is the covariance between them. c_1 and c_2 are two constants dependent on the range of pixel values.

IV. RESULTS

A. Studies on the fastMRI Multi-Coil Knee Dataset

In this section, we show the result of applying our optimized scan-adaptive SUNO masks on the fastMRI multi-coil knee dataset at $4\times$ and $8\times$ acceleration factors. We compare the quality of the reconstructed images using our optimized masks with the other baseline masks described in section III-B. Figure 4 shows the images reconstructed using MoDL network (along with zoom-ins over a region of interest) using SUNO mask along with low-frequency, VDRS, equispaced, SeqMRI, and LOUPE masks at $4\times$ acceleration factor, respectively. It is clear from the figure that the proposed SUNO approach (both global and local) gives better-reconstructed images compared to other baselines in terms of NRMSE, SSIM, and PSNR metrics. The zoom-ins also show that the reconstructed image using the SUNO mask preserves the fine structural detail present in the ground truth. Figure 5 shows the reconstructed and error images at $8\times$ acceleration factor using the SUNO-Local and SUNO-Global approaches along with the other baselines. The error images show the least reconstructed error using the SUNO approach (both global and local) compared to other baselines. Table II shows the mean and standard deviation values of NRMSE, SSIM, and PSNR for reconstructed images using three different approaches: ZS-SSL [58], E2E-VarNet [25], and MoDL [28]. These and all subsequent test experiments use these three models, post-trained on fixed or optimized masks at each acceleration factor. From the table, we can see that the proposed SUNO local and global approaches outperform the rest on average over the entire test set for all three reconstructors. The local network training was implemented and demonstrated for the E2E-VarNet and MoDL reconstruction network. The ZS-SSL framework employed for comparison operates in an unsupervised learning setting, where the concept of supervised local training is not applicable.

B. Applicability to Different Anatomies

To test the applicability of our proposed scan-adaptive sampling prediction approach on different anatomies, we also optimized masks using the proposed training pipeline on

³<https://github.com/facebookresearch/fastMRI/blob/main/fastmri/models/varnet.py>

⁴<https://github.com/byaman14/ZS-SSL-PyTorch>

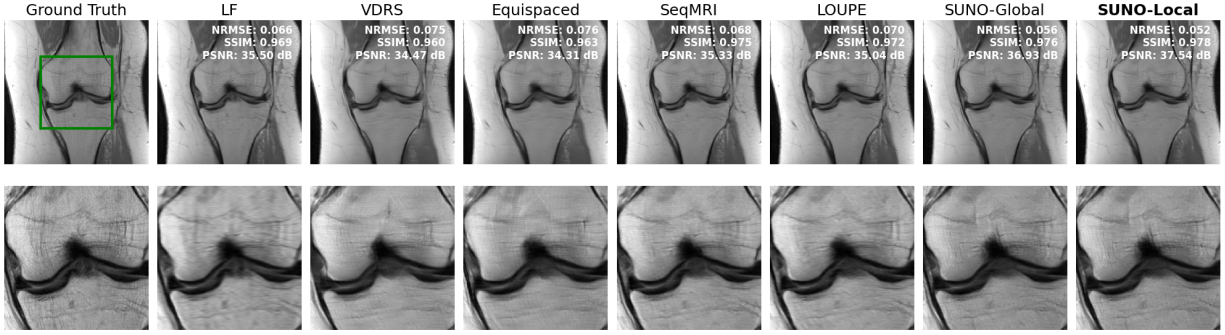


Fig. 4: Reconstructed images using MoDL network at $4\times$ acceleration factor for a testing slice. The second row shows the zoom-in images from the area inside the green rectangle which shows that both the SUNO-Local and SUNO-Global approach outperforms the rest in terms of visual quality and better preserves structural detail.

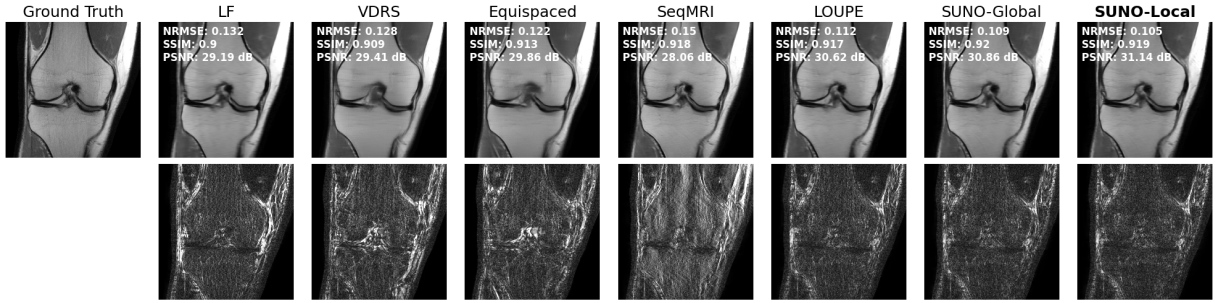


Fig. 5: Reconstructed images using MoDL network at $8\times$ acceleration factor for a testing slice. The second row shows the error maps which show that both the SUNO-Local and SUNO-Global outperform the rest in terms of visual quality and preserve structural details better. The error images (magnitudes) shown are in the range $[0, 0.1]$

the fastMRI multi-coil brain dataset. Then, using the nearest neighbor search, the masks were predicted at test time, and the performance of these learned SUNO masks was compared with the other baselines - low-frequency, VDRS, equispaced, SeqMRI, and LOUPE masks.

Figure 6 and 7 show the reconstructed and error images using a brain testing slice for $4\times$ and $8\times$ acceleration factors. The figure shows that the optimized scan adaptive SUNO masks outperform the other baseline masks in terms of the reconstruction metrics for both $4\times$ and $8\times$ acceleration factors. The error images indicate a lower reconstruction error for both the SUNO local and global approaches. The mean and standard deviation values of the reconstruction metrics using ZS-SSL, VarNet, and MoDL reconstruction methods learned over all test cases are mentioned in Table III. From the table, we can see that the proposed SUNO local and global approaches outperformed all baselines for all three reconstruction approaches in terms of the error metrics used.

C. Comparison with the Oracle Case

In this section, we compare the performance of oracle masks optimized directly on the test slices (using the sampling optimization with a fixed reconstructor) with the ones predicted from the nearest neighbor search (SUNO masks). Table IV gives a comparison of the oracle and SUNO masks for the fastMRI knee dataset. We observe that the oracle-optimized

masks perform better than the SUNO mask for both acceleration factors, as expected. This is because the oracle mask was optimized for the particular test scan (scan-adaptive) while the SUNO mask uses the mask optimized on the nearest neighbor training scan. Hence, the oracle masks perform slightly better in general. However, we want to emphasize that estimating the oracle masks requires access to the ground truth, making it infeasible at test time.

D. Ablation Study - Convergence and Choice of Parameters for the Sampling Optimization Algorithm

In this section, we show the effect of changing different parameters for running the ICD sampling optimization (Algorithm 1) on the optimized SUNO masks for the fastMRI multi-coil knee dataset.

1) *Effect of initialization:* In this section, we explore the effect of changing the initial mask used for the sampling pattern optimization - VDRS [8] and LOUPE [38] masks. The algorithm, when started with a particular mask and given a choice of reconstruction method and loss used, could give different solutions. Table V lists the performance metrics for the images reconstructed using SUNO masks optimized from a) VDRS mask and b) LOUPE mask with the MoDL reconstruction network. Figure 8 shows one such example of the reconstructed images obtained from SUNO masks initialized using LOUPE and VDRS masks. From the results, we observe that the sampling optimization initialized with the LOUPE

Reconstructor	Mask	4x			8x		
		NRMSE ↓	SSIM ↑	PSNR (dB) ↑	NRMSE ↓	SSIM ↑	PSNR (dB) ↑
ZS-SSL [58]	LF	0.156 ± 0.074	0.794 ± 0.072	29.15 ± 2.80	0.251 ± 0.099	0.812 ± 0.067	24.72 ± 2.80
	VDRS [8]	0.125 ± 0.052	0.834 ± 0.074	30.94 ± 2.87	0.187 ± 0.060	0.814 ± 0.047	27.02 ± 1.91
	Equispaced [15]	0.119 ± 0.053	0.841 ± 0.070	31.62 ± 2.94	0.210 ± 0.053	0.827 ± 0.043	25.85 ± 1.53
	SeqMRI [43]	0.118 ± 0.040	0.846 ± 0.081	30.07 ± 2.89	0.191 ± 0.075	0.844 ± 0.080	27.11 ± 3.11
	LOUPE [38]	0.114 ± 0.057	0.848 ± 0.071	31.70 ± 3.22	0.180 ± 0.082	0.846 ± 0.041	27.65 ± 2.42
	SUNO-Global (Ours)	0.110 ± 0.058	0.860 ± 0.081	32.08 ± 3.43	0.166 ± 0.067	0.854 ± 0.039	28.96 ± 2.23
E2E-VarNet [25]	LF	0.127 ± 0.056	0.867 ± 0.051	30.62 ± 2.66	0.198 ± 0.069	0.780 ± 0.065	27.41 ± 2.59
	VDRS	0.124 ± 0.047	0.864 ± 0.054	30.66 ± 2.50	0.186 ± 0.064	0.801 ± 0.065	27.67 ± 2.49
	Equispaced	0.110 ± 0.043	0.875 ± 0.053	31.75 ± 2.58	0.182 ± 0.061	0.812 ± 0.059	27.86 ± 2.33
	SeqMRI	0.109 ± 0.046	0.894 ± 0.049	31.90 ± 2.60	0.159 ± 0.051	0.830 ± 0.058	28.85 ± 1.97
	LOUPE	0.107 ± 0.046	0.892 ± 0.049	32.07 ± 2.70	0.154 ± 0.059	0.824 ± 0.062	29.27 ± 2.37
	SUNO-Global (Ours)	0.101 ± 0.045	0.898 ± 0.051	32.67 ± 2.94	0.149 ± 0.056	0.825 ± 0.061	29.58 ± 2.28
MoDL [28]	SUNO-Local (Ours)	0.100 ± 0.044	0.901 ± 0.052	32.72 ± 2.89	0.148 ± 0.054	0.827 ± 0.063	29.76 ± 2.30
	LF	0.134 ± 0.066	0.929 ± 0.031	30.59 ± 3.05	0.203 ± 0.064	0.884 ± 0.041	27.34 ± 2.77
	VDRS [8]	0.137 ± 0.051	0.920 ± 0.031	31.08 ± 2.50	0.208 ± 0.065	0.873 ± 0.038	26.66 ± 2.26
	Equispaced [15]	0.127 ± 0.050	0.927 ± 0.031	30.67 ± 2.58	0.201 ± 0.067	0.878 ± 0.042	27.00 ± 2.27
	SeqMRI [43]	0.118 ± 0.048	0.939 ± 0.028	31.50 ± 2.79	0.186 ± 0.065	0.900 ± 0.035	27.75 ± 2.45
	LOUPE [38]	0.116 ± 0.049	0.938 ± 0.028	31.63 ± 2.81	0.178 ± 0.072	0.900 ± 0.039	28.34 ± 2.78
	SUNO-Global (Ours)	0.114 ± 0.046	0.940 ± 0.029	31.74 ± 2.85	0.172 ± 0.065	0.901 ± 0.039	28.54 ± 2.61
	SUNO-Local (Ours)	0.110 ± 0.045	0.941 ± 0.029	32.07 ± 2.83	0.170 ± 0.066	0.902 ± 0.039	28.70 ± 2.66

TABLE II: Distribution of NRMSE, SSIM, and PSNR values for the reconstructed images from the multicoil knee dataset at 4x and 8x acceleration factors using various masks and reconstructors. The SUNO approaches had better quality metrics than the rest at both acceleration factors for all three reconstruction methods used.

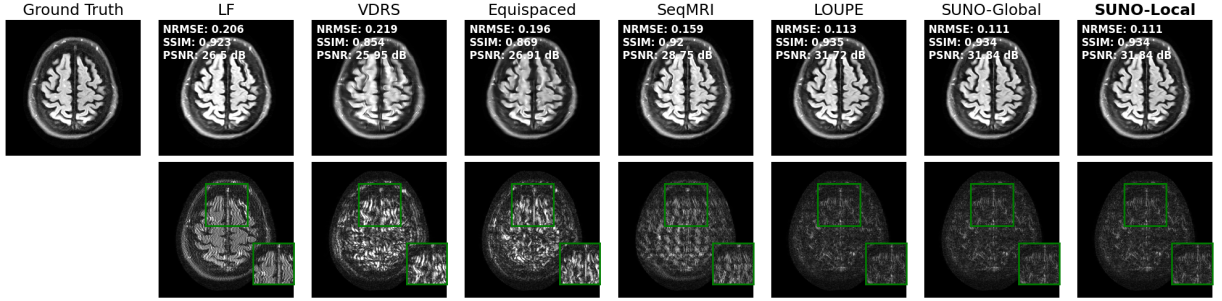


Fig. 6: Reconstructed and error images using different undersampling patterns using MoDL reconstruction network (two-channel) on fastMRI brain dataset at 4x acceleration factor. The green rectangle shows the zoomed-in portions in the error image. The proposed SUNO approach performed better than other baselines in terms of NRMSE, SSIM, and PSNR metrics.

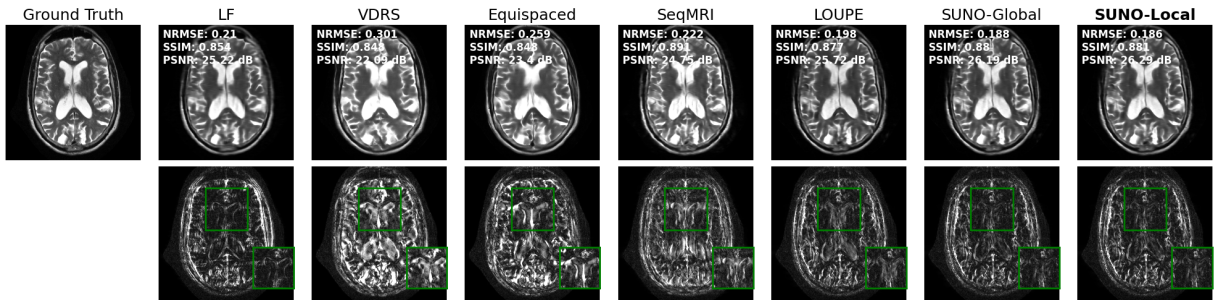


Fig. 7: Reconstructed and error images using different undersampling patterns using MoDL reconstruction network (two-channel) on fastMRI brain dataset at 8x acceleration factor. The green rectangle shows the zoomed-in portions in the error image. The proposed SUNO approach performed better than other baselines in terms of NRMSE, SSIM, and PSNR metrics.

mask results in a better reconstruction compared to when it is initialized with a VDRS mask. Since the LOUPE mask is already optimized for multiple training scans (population adaptive), it acts as a better initial point for starting the sampling optimization. The algorithm further optimizes the LOUPE mask for scan-specific details, hence, we get better performance with it compared to LOUPE on test scans.

2) *Effect of reconstruction method*: This section shows the effect of the reconstruction method used inside the Algorithm 1 on the quality of optimized SUNO masks. The algorithm works for any choice of reconstruction method, e.g., compressed sensing (CS) or a pre-trained deep learning model (e.g., U-Net, MoDL, or E2E-VarNet [24], [25]). In this paper, we show masks optimized using two such methods - U-Net

Reconstructor	Mask	4x			8x		
		NRMSE ↓	SSIM ↑	PSNR (dB) ↑	NRMSE ↓	SSIM ↑	PSNR (dB) ↑
ZS-SSL [58]	LF	0.173 ± 0.057	0.854 ± 0.025	29.14 ± 2.46	0.259 ± 0.067	0.764 ± 0.046	25.45 ± 2.14
	VDRS [8]	0.124 ± 0.034	0.904 ± 0.029	31.83 ± 2.50	0.241 ± 0.065	0.802 ± 0.061	26.07 ± 2.37
	Equispaced [15]	0.120 ± 0.032	0.891 ± 0.028	32.13 ± 2.30	0.297 ± 0.053	0.742 ± 0.049	24.09 ± 1.36
	SeqMRI [43]	0.118 ± 0.027	0.897 ± 0.025	32.22 ± 2.76	0.171 ± 0.060	0.841 ± 0.029	27.98 ± 2.06
	LOUPE [38]	0.114 ± 0.024	0.900 ± 0.021	32.61 ± 2.20	0.166 ± 0.037	0.864 ± 0.025	28.94 ± 1.93
	SUNO-Global (Ours)	0.111 ± 0.025	0.903 ± 0.020	32.83 ± 2.02	0.158 ± 0.040	0.869 ± 0.024	29.35 ± 1.92
E2E-VarNet [25]	LF	0.144 ± 0.047	0.964 ± 0.012	30.74 ± 2.63	0.210 ± 0.054	0.927 ± 0.025	27.45 ± 2.24
	VDRS [8]	0.116 ± 0.025	0.970 ± 0.010	32.37 ± 1.89	0.194 ± 0.029	0.934 ± 0.022	27.95 ± 1.91
	Equispaced [15]	0.118 ± 0.022	0.970 ± 0.009	32.20 ± 1.64	0.201 ± 0.037	0.932 ± 0.021	27.69 ± 2.10
	SeqMRI [43]	0.109 ± 0.026	0.973 ± 0.008	33.01 ± 2.09	0.159 ± 0.033	0.958 ± 0.011	29.45 ± 1.58
	LOUPE [38]	0.104 ± 0.024	0.978 ± 0.006	33.40 ± 2.09	0.156 ± 0.031	0.957 ± 0.011	29.91 ± 1.72
	SUNO-Global (Ours)	0.102 ± 0.023	0.978 ± 0.006	33.51 ± 2.09	0.153 ± 0.028	0.958 ± 0.010	30.07 ± 1.68
MoDL [28]	SUNO-Local (Ours)	0.101 ± 0.022	0.980 ± 0.006	33.65 ± 2.10	0.151 ± 0.027	0.960 ± 0.009	30.85 ± 1.72
	LF	0.154 ± 0.046	0.956 ± 0.014	30.22 ± 2.57	0.230 ± 0.066	0.897 ± 0.042	26.36 ± 1.98
	VDRS [8]	0.175 ± 0.052	0.938 ± 0.019	29.28 ± 2.20	0.242 ± 0.071	0.892 ± 0.039	25.77 ± 2.24
	Equispaced [15]	0.156 ± 0.038	0.941 ± 0.020	29.93 ± 2.01	0.248 ± 0.051	0.889 ± 0.038	25.51 ± 1.68
	SeqMRI [43]	0.122 ± 0.035	0.958 ± 0.017	31.87 ± 2.15	0.190 ± 0.046	0.926 ± 0.016	27.96 ± 1.73
	LOUPE [38]	0.119 ± 0.033	0.962 ± 0.014	31.65 ± 2.26	0.186 ± 0.046	0.922 ± 0.033	28.21 ± 1.62
	SUNO-Global (Ours)	0.117 ± 0.031	0.962 ± 0.013	32.10 ± 2.20	0.184 ± 0.046	0.922 ± 0.032	28.30 ± 1.59
	SUNO-Local (Ours)	0.115 ± 0.030	0.963 ± 0.012	32.59 ± 2.17	0.182 ± 0.040	0.923 ± 0.032	28.40 ± 1.40

TABLE III: Distribution of NRMSE, SSIM, and PSNR values for the reconstructed images from the multicoil brain dataset at 4x and 8x acceleration factors using various masks and reconstructors. The SUNO approach outperforms the rest at both acceleration factors for all three reconstruction methods used. The values displayed are mean \pm std.

Acceleration Factor	4 \times	8 \times
Oracle	0.110/0.941/32.07	0.149/0.902/29.60
SUNO	0.114/0.940/31.74	0.172/0.901/28.54

TABLE IV: Comparison of the oracle and SUNO masks on the fastMRI knee dataset on the test cases. The values shown are mean NRMSE/SSIM/PSNR.

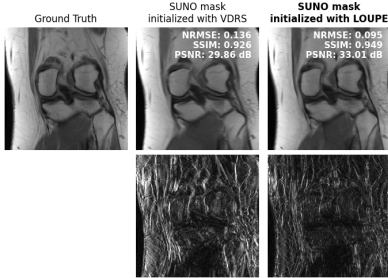


Fig. 8: Comparing reconstructed images using SUNO masks initialized from LOUPE and VDRS masks at 8 \times acceleration factor.

and MoDL and compare the reconstructed images using these masks. Figure 9 shows the U-Net and MoDL reconstructed images using two optimized masks: one that used U-Net as the reconstruction model in the sampling optimization algorithm and the other with MoDL. The figure shows that we get the best reconstruction when a better reconstructor (i.e., MoDL network) is used both as the reconstruction model inside the sampling optimization and as the final reconstructor method.

E. Computational Cost of Proposed Approaches

This section discusses the time complexity of our proposed algorithms: 1) the sampling optimization algorithm and 2) the nearest neighbor search.

1) *Complexity of Algorithm 1*: In this section, we show the effect of different parameters on the run time required for the sampling pattern optimization algorithm. The algorithm learns

Initial Mask Chosen	NRMSE	SSIM	PSNR
VDRS	0.164	0.896	28.45
LOUPE	0.142	0.903	29.78

TABLE V: Mean values of reconstruction metrics for masks initialized with VDRS and LOUPE at an 8 \times acceleration factor, evaluated over 50 test cases. The sampling optimization, when initialized with the LOUPE mask, results in better reconstruction quality.

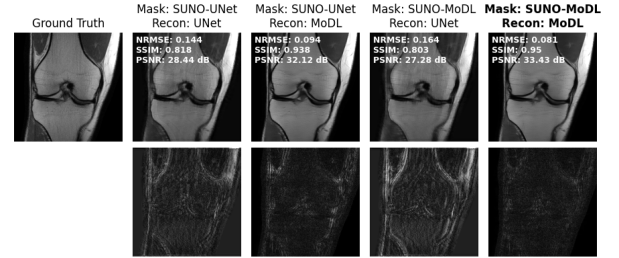


Fig. 9: Comparison of reconstructed images from masks optimized using 1) U-Net and 2) MoDL as the reconstruction model. For each mask, the reconstructed images using both the U-Net and MoDL networks is shown.

a unique mask for each training scan and slice, and as a result, An important thing to consider as part of the training pipeline is the computational complexity of the algorithm. Some of the parameters affecting runtime for the algorithm 1 are the reconstruction method that is run repeatedly while moving sampling lines or phase encodes in the mask and the underlying undersampling factor. Table VI shows the dependence of the runtime on both these parameters. It is clear from the table that the sampling optimization algorithm using a U-Net reconstruction model results in a lower runtime compared to running the algorithm using a MoDL reconstructor. This is because the MoDL reconstruction network uses multiple unrollings of the denoiser and the CG block [28].

Reconstructor Used	4×	8×
U-Net	25.3	13.3
MoDL	52.1	28.6

TABLE VI: Time required (minutes) for running one pass of Algorithm 1 (offline). Separate times are shown for U-Net and MoDL reconstructors at 4× and 8× acceleration factors. The algorithm was run on an NVIDIA RTX A5000 GPU with 24 GB RAM.

2) *Cost of Nearest Neighbor Search*: In this section, we discuss the time complexity of neighbor search and local MoDL network training. Table VII shows the time involved in finding the nearest neighbors for selecting the SUNO mask from the training set, the time taken to find neighbors for local network training, and the corresponding local network training time (with 30 images). Note that all these steps (except selecting the nearest neighbor mask) are post-processing (i.e., after the initial scan of low-frequency phase encoding lines has been collected). Also, the testing/inference time with the trained local MoDL network is the same as for the pre-trained (global) MoDL since the network architecture remains the same.

Procedure	Nearest Neighbor Mask Selection	Neighborhood Selection for Local Training	Local Network Training	Inference
Time	0.85	0.85	400	1.53

TABLE VII: Time taken (in seconds) for various procedures involved in the neighbor selection, network training, and inference. Local network training and inference steps are offline since they will be done after the data is acquired.

V. DISCUSSION

We proposed a novel way of learning scan-adaptive Cartesian undersampling patterns for multi-coil MRI setting. The proposed method was shown to have better accuracy than the currently used population-based 1D Cartesian undersampling patterns in terms of NRMSE, SSIM, and PSNR metrics as well as the visual quality at 4x and 8x acceleration factors. The zoomed-in images show better features in the reconstructed images using the proposed SUNO masks compared to other baselines. The proposed method was tested on two different anatomies - the knee and the brain - and its generalization was indicated for different datasets. Similar to the greedy algorithm in prior work [35], the sampling optimization algorithm can be used along with any choice of reconstruction method and the loss metric, giving freedom in designing sampling patterns for different anatomies and different acceleration factors. A nearest neighbor search was used to predict the pattern at test time from the dictionary of learned patterns. Furthermore, a local network was trained in the neighborhood of the test image, yielding even better accuracy at test time than a global network trained on the whole training set.

A drawback of the current method is the time-consuming process of learning scan-adaptive sampling patterns on the whole training set. More work is required to make the optimization process efficient and faster, to make this approach

more feasible. However, since this sampling optimization is part of the offline training module, it does not affect the acquisition and sampling prediction at test time, which is 0.85 seconds in our experiments.

VI. CONCLUSION

In this work, we proposed a novel MRI sampling prediction algorithm for multi-coil MRI that estimates a collection of scan-adaptive sampling patterns and a reconstruction network trained on those patterns alternately, at the training time. The proposed algorithm was validated on the publicly available fastMRI knee and brain dataset and was shown to have better reconstruction accuracy than currently used Cartesian undersampling patterns. This study demonstrated the advantages of employing scan-adaptive masks by providing evidence that they are more effectively tailored to individual patients than population-adaptive masks. We also showed the dependence of the learned sampling patterns on acceleration factors, the initialization of the sampling algorithm, and the reconstruction method used. Future work will include employing deep image prior or other scan-adaptive MRI reconstructions in our framework, extending the approach to cardiac MRI, and/or predicting sparse views for X-ray CT reconstruction.

VII. ACKNOWLEDGMENTS

The authors would like to acknowledge Dr. Maryam Sayadi, Michigan State University for her inputs throughout the project. The authors also acknowledge Evan Bell and Shijun Liang from Michigan State University, and Zhishen Huang from Amazon Inc. for useful discussions.

REFERENCES

- [1] Z. Liang and P.C. Lauterbur, *Principles of magnetic resonance Imaging*, SPIE Optical Engineering Press Bellingham, WA, 2000.
- [2] M.A. Bernstein, K.F. King, and X.J. Zhou, *Handbook of MRI pulse sequences*, Elsevier, 2004.
- [3] J. Tsao, "Ultrafast imaging: principles, pitfalls, solutions, and applications," *Journal of Mag. Reson. Img.*, vol. 32, no. 2, pp. 252–266, 2010.
- [4] K.P. Pruessmann, "Encoding and reconstruction in parallel MRI," *NMR in Biomedicine*, vol. 19, no. 3, pp. 288–299, 2006.
- [5] L. Ying and Z. Liang, "Parallel MRI using phased array coils," *IEEE Signal Processing Magazine*, vol. 27, no. 4, pp. 90–98, 2010.
- [6] A. Deshmane, V. Gulani, M.A. Griswold, and N. Seiberlich, "Parallel MR img.," *Journal of Mag. Reson. Img.*, vol. 36, no. 1, pp. 55–72, 2012.
- [7] D.L. Donoho, "Compressed sensing," *IEEE Trans. on information theory*, vol. 52, no. 4, pp. 1289–1306, 2006.
- [8] M. Lustig, D. Donoho, and J.M. Pauly, "Sparse MRI: The application of compressed sensing for rapid MR img.," *Magn. Reson. in Med.*, vol. 58, no. 6, pp. 1182–1195, 2007.
- [9] E.J. Candes and T. Tao, "Near-optimal signal recovery from random projections: Universal encoding strategies?," *IEEE Trans. on information theory*, vol. 52, no. 12, pp. 5406–5425, 2006.
- [10] E. Candes and J. Romberg, "Sparsity and incoherence in compressive sampling," *Inverse problems*, vol. 23, no. 3, pp. 969, 2007.
- [11] M. Lustig, D.L. Donoho, J.M. Santos, and J.M. Pauly, "Compressed sensing MRI," *IEEE signal processing magazine*, vol. 25, no. 2, pp. 72–82, 2008.
- [12] Z. Wang and G.R. Arce, "Variable density compressed image sampling," *IEEE Trans. on image processing*, vol. 19, no. 1, pp. 264–270, 2009.
- [13] M. Murphy, M. Alley, J. Demmel, K. Keutzer, S. Vasanawala, and M. Lustig, "Fast 11-spirit compressed sensing parallel imaging MRI: scalable parallel implementation and clinically feasible runtime," *IEEE Trans. on Med. Img.*, vol. 31, no. 6, pp. 1250–1262, 2012.

- [14] E. Levine, B. Daniel, S. Vasanawala, B. Hargreaves, and M. Saranathan, "3d cartesian MRI with compressed sensing and variable view sharing using complementary poisson-disc sampling," *Magn. Reson. in Med.*, vol. 77, no. 5, pp. 1774–1785, 2017.
- [15] J.P. Haldar, D. Hernando, and Z. Liang, "Compressed-sensing MRI with random encoding," *IEEE Trans. on Med. Img.*, vol. 30, no. 4, pp. 893–903, 2010.
- [16] S. Ravishankar and Y. Bresler, "MR image reconstruction from highly undersampled k-space data by dictionary learning," *IEEE Trans. on Med. Img.*, vol. 30, no. 5, pp. 1028–1041, 2010.
- [17] S.G. Lingala and M. Jacob, "Blind compressive sensing dynamic MRI," *IEEE Trans. on Med. Img.*, vol. 32, no. 6, pp. 1132–1145, 2013.
- [18] X. Qu, Y. Hou, F. Lam, D. Guo, J. Zhong, and Z. Chen, "Magnetic resonance image reconstruction from undersampled measurements using a patch-based nonlocal operator," *Med. image analysis*, vol. 18, no. 6, pp. 843–856, 2014.
- [19] Z. Zhan, J. Cai, D. Guo, Y. Liu, Z. Chen, and X. Qu, "Fast multiclass dictionaries learning with geometrical directions in MRI reconstruction," *IEEE Trans. on bioMed. engineering*, vol. 63, no. 9, pp. 1850–1861, 2015.
- [20] S. Ravishankar and Y. Bresler, "Learning sparsifying transforms," *IEEE Trans. on Signal Processing*, vol. 61, no. 5, pp. 1072–1086, 2012.
- [21] S. Ravishankar, J.C. Ye, and J.A. Fessler, "Image reconstruction: From sparsity to data-adaptive methods and machine learning," *Proceedings of the IEEE*, vol. 108, no. 1, pp. 86–109, 2019.
- [22] O. Ronneberger, P. Fischer, and T. Brox, "U-Net: Convolutional networks for biomed. image segmentation," in *International Conference on Med. image computing and computer-assisted intervention*. Springer, 2015, pp. 234–241.
- [23] C.M. Hyun, H.P. Kim, S.M. Lee, S. Lee, and J.K. Seo, "Deep learning for undersampled MRI reconstruction," *Physics in Medicine & Biology*, vol. 63, no. 13, pp. 135007, 2018.
- [24] K. Hammernik, T. Klatzer, E. Kobler, M.P. Recht, D.K. Sodickson, F. Knoll, and F. Knoll, "Learning a variational network for reconstruction of accelerated MRI data," *Magn. Reson. in Med.*, vol. 79, no. 6, pp. 3055–3071, 2018.
- [25] A. Sriram, J. Zbontar, T. Murrell, A. Defazio, C.L. Zitnick, N. Yakubova, C.M. Hyun, H.P. Kim, S.M. Lee, S. Lee, and J.K. Seo, "Deep learning for undersampled MRI reconstruction," in *Med. Image Computing and Computer Assisted Intervention—MICCAI 2020: 23rd International Conference, Lima, Peru, October 4–8, 2020, Proceedings, Part II 23*. Springer, 2020, pp. 64–73.
- [26] J. Sun, H. Li, Z. Xu, et al., "Deep ADMM-Net for compressive sensing MRI," *Advances in neural information processing systems*, vol. 29, 2016.
- [27] M. Mardani, E. Gong, J.Y. Cheng, S. Vasanawala, G. Zaharchuk, M. Alley, N. Thakur, S. Han, W. Dally, J.M. Pauly, et al., "Deep generative adversarial networks for compressed sensing automates MRI," *arXiv preprint arXiv:1706.00051*, 2017.
- [28] H.K. Aggarwal, M.P. Mani, and M. Jacob, "MoDL: Model-based deep learning architecture for inverse problems," *IEEE Trans. on Med. Img.*, vol. 38, no. 2, pp. 394–405, 2018.
- [29] S. Ravishankar and Y. Bresler, "Adaptive sampling design for compressed sensing MRI," in *2011 Annual International Conference of the IEEE Engineering in Medicine and Biology Society*. IEEE, 2011, pp. 3751–3755.
- [30] F. Knoll, C. Clason, C. Diwok, and R. Stollberger, "Adapted random sampling patterns for accelerated MRI," *Magnetic resonance materials in physics, biology and medicine*, vol. 24, pp. 43–50, 2011.
- [31] J. Vellagoundar and R.R. Machireddy, "A robust adaptive sampling method for faster acquisition of MR images," *Magnetic resonance Img.*, vol. 33, no. 5, pp. 635–643, 2015.
- [32] Y. Zhang, B.S. Peterson, G. Ji, and Z. Dong, "Energy preserved sampling for compressed sensing MRI," *Computational and mathematical methods in medicine*, vol. 2014, no. 1, pp. 546814, 2014.
- [33] J.P. Haldar and D. Kim, "OEDIPUS: An experiment design framework for sparsity-constrained MRI," *IEEE Trans. on Med. Img.*, vol. 38, no. 7, pp. 1545–1558, 2019.
- [34] M. Seeger, H. Nickisch, R. Pohmann, and Bernhard Schölkopf, "Optimization of k-space trajectories for compressed sensing by bayesian experimental design," *Magn. Reson. in Med.*, vol. 63, no. 1, pp. 116–126, 2010.
- [35] B. Gözcü, R. K. Mahabadi, Y. Li, E. Ilıcak, T. Cukur, J. Scarlett, and V. Cevher, "Learning-based compressive MRI," *IEEE Trans. on Med. Img.*, vol. 37, no. 6, pp. 1394–1406, 2018.
- [36] B. Gözcü, T. Sanchez, and V. Cevher, "Rethinking sampling in parallel MRI: A data-driven approach," in *2019 27th European Signal Processing Conference (EUSIPCO)*. IEEE, 2019, pp. 1–5.
- [37] T. Sanchez, B. Gözcü, R. van Heeswijk, A. Eftekhari, E. Ilıcak, T. Çukur, and V. Cevher, "Scalable learning-based sampling optimization for compressive dynamic MRI," in *2020 IEEE International Conference on Acoustics, Speech and Signal Processing (ICASSP)*. IEEE, 2020, pp. 8584–8588.
- [38] C.D. Bahadir, A.Q. Wang, A.V. Dalca, and M.R. Sabuncu, "Deep-learning-based optimization of the under-sampling pattern in MRI," *IEEE Trans. on Computational Img.*, vol. 6, pp. 1139–1152, 2020.
- [39] J. Zhang, H. Zhang, A. Wang, Q. Zhang, M. Sabuncu, P. Spincemaille, T.D. Nguyen, and Y. Wang, "Extending LOUPE for k-space under-sampling pattern optimization in multi-coil MRI," in *Machine Learning for Med. Image Reconstruction: Third International Workshop, MLMIR 2020, Lima, Peru, October 8, 2020, Proceedings 3*. Springer, 2020, pp. 91–101.
- [40] H.K. Aggarwal and M. Jacob, "J-MoDL: Joint model-based deep learning for optimized sampling and reconstruction," *IEEE journal of selected topics in signal processing*, vol. 14, no. 6, pp. 1151–1162, 2020.
- [41] F. Sherry, M. Benning, J.C. De los Reyes, M.J. Graves, G. Maierhofer, G. Williams, Carola-Bibiane Schönlieb, and Matthias J Ehrhardt, "Learning the sampling pattern for MRI," *IEEE Trans. on Med. Img.*, vol. 39, no. 12, pp. 4310–4321, 2020.
- [42] M.V. Zibetti, G.T. Herman, and R.R. Regatte, "Fast data-driven learning of parallel MRI sampling patterns for large scale problems," *Scientific Reports*, vol. 11, no. 1, pp. 19312, 2021.
- [43] T. Yin, Z. Wu, H. Sun, A.V. Dalca, Y. Yue, and K.L. Bouman, "End-to-end sequential sampling and reconstruction for MR img.," in *Proceedings of the Machine Learning for Health Conference*, 2021.
- [44] M.V.W. Zibetti, F. Knoll, and R.R. Regatte, "Alternating learning approach for variational networks and undersampling pattern in parallel MRI applications," *IEEE Trans. on Computational Img.*, vol. 8, pp. 449–461, 2022.
- [45] Z. Huang and S. Ravishankar, "Single-pass object-adaptive data under-sampling and reconstruction for MRI," *IEEE Trans. on Computational Img.*, vol. 8, pp. 333–345, 2022.
- [46] C. Alkan, M. Mardani, C. Liao, Z. Li, S.S. Vasanawala, and J.M. Pauly, "Autosamp: Autoencoding k-space sampling via variational information maximization for 3D MRI," *IEEE Trans. on Med. Img.*, 2024.
- [47] T. Weiss, O. Senouf, S. Vedula, O. Michailovich, M. Zibulevsky, and A. Bronstein, "Pilot: Physics-informed learned optimized trajectories for accelerated mri," *arXiv preprint arXiv:1909.05773*, 2019.
- [48] C. Lazarus, P. Weiss, N. Chauffert, F. Mauconduit, L. El Gueddari, C. Destrieux, I. Zemmoura, A. Vignaud, and P. Ciuciu, "Sparkling: variable-density k-space filling curves for accelerated t2*-weighted MRI," *Magn. Reson. in Med.*, vol. 81, no. 6, pp. 3643–3661, 2019.
- [49] GR Chaithya, P. Weiss, G. Daval-Frérôt, A. Massire, A. Vignaud, and P. Ciuciu, "Optimizing full 3d sparkling trajectories for high-resolution magnetic resonance imaging," *IEEE Transactions on Medical Imaging*, vol. 41, no. 8, pp. 2105–2117, 2022.
- [50] G. Wang, T. Luo, J. Nielsen, D.C. Noll, and J.A. Fessler, "B-spline parameterized joint optimization of reconstruction and k-space trajectories (BJORK) for accelerated 2D MRI," *IEEE Trans. on Med. Img.*, vol. 41, no. 9, pp. 2318–2330, 2022.
- [51] Zaccharie Ramzi, GR Chaithya, Jean-Luc Starck, and Philippe Ciuciu, "NC-PDNet: A density-compensated unrolled network for 2D and 3D non-cartesian MRI reconstruction," *IEEE Transactions on Medical Imaging*, vol. 41, no. 7, pp. 1625–1638, 2022.
- [52] G. Wang, J. F. Nielsen, J. A. Fessler, and D. C. Noll, "Stochastic optimization of three-dimensional non-cartesian sampling trajectory," *Magn. Reson. in Med.*, vol. 90, no. 2, pp. 417–431, 2023.
- [53] L. Pineda, S. Basu, A. Romero, R. Calandra, and M. Drozdal, "Active MR k-space sampling with reinforcement learning," in *Med. Image Computing and Computer Assisted Intervention—MICCAI 2020: 23rd International Conference, Lima, Peru, October 4–8, 2020, Proceedings, Part II 23*. Springer, 2020, pp. 23–33.
- [54] T. Bakker, H. van Hoof, and M. Welling, "Experimental design for MRI by greedy policy search," *Advances in Neural Information Processing Systems*, vol. 33, pp. 18954–18966, 2020.
- [55] Z. Wang, A.C. Bovik, H.R. Sheikh, and E.P. Simoncelli, "Image quality assessment: from error visibility to structural similarity," *IEEE Trans. on image processing*, vol. 13, no. 4, pp. 600–612, 2004.
- [56] S. Liang, A. Lahiri, and S. Ravishankar, "Adaptive local neighborhood-based neural networks for MR image reconstruction from undersampled data," *IEEE Trans. on Computational Img.*, 2024.
- [57] S. Gautam, A. Li, and S. Ravishankar, "Patient-adaptive and learned MRI data undersampling using neighborhood clustering," in *2024 IEEE International Conference on Acoustics, Speech and Signal Processing (ICASSP)*. IEEE, 2024, pp. 2081–2085.

- [58] Burhaneddin Yaman, Seyed Amir Hossein Hosseini, and Mehmet Akcakaya, “Zero-shot self-supervised learning for MRI reconstruction,” in *International Conference on Learning Representations*, 2022.
- [59] J. Zbontar, F. Knoll, A. Sriram, T. Murrell, Z. Huang, M.J. Muckley, A. Defazio, R. Stern, P. Johnson, M. Bruno, et al., “fastMRI: An open dataset and benchmarks for accelerated MRI,” *arXiv preprint arXiv:1811.08839*, 2018.
- [60] F. Knoll, J. Zbontar, A. Sriram, M.J. Muckley, M. Bruno, A. Defazio, M. Parente, K.J. Geras, J. Katsnelson, H. Chandarana, et al., “fastMRI: A publicly available raw k-space and dicom dataset of knee images for accelerated MR image reconstruction using machine learning,” *Radiology: Artificial Intelligence*, vol. 2, no. 1, pp. e190007, 2020.
- [61] M. Uecker, P. Lai, M.J. Murphy, P. Virtue, M. Elad, J.M. Pauly, S.S. Vasanawala, and M. Lustig, “ESPIRiT — an eigenvalue approach to autocalibrating parallel MRI: where SENSE meets GRAPPA,” *Magn. Reson. in Med.*, vol. 71, no. 3, pp. 990–1001, 2014.
- [62] S. Yu, B. Park, and J. Jeong, “Deep iterative down-up CNN for image denoising,” in *Proceedings of the IEEE/CVF conference on computer vision and pattern recognition workshops*, 2019.
- [63] D.P. Kingma and J. Ba, “Adam: A method for stochastic optimization,” *arXiv preprint arXiv:1412.6980*, 2014.